RESEARCH ARTICLE

Extended model predictive control scheme for smooth path following of autonomous vehicles

Qianjie LIU[a], Shuang SONG[a], Huosheng HU[b], Tengchao HUANG[a], Chenyang LI[a], Qingyuan ZHU (✉)[a]

[a] *Department of Mechanical and Electrical Engineering, Xiamen University, Xiamen 361102, China*
[b] *School of Computer Science and Electronic Engineering, University of Essex, Colchester CO4 3SQ, UK*

✉ *Corresponding author. E-mail: zhuqy@xmu.edu.cn (Qingyuan ZHU)*

ABSTRACT   This paper presents an extended model predictive control (MPC) scheme for implementing optimal path following of autonomous vehicles, which has multiple constraints and an integrated model of vehicle and road dynamics. Road curvature and inclination factors are used in the construction of the vehicle dynamic model to describe its lateral and roll dynamics accurately. Sideslip, rollover, and vehicle envelopes are used as multiple constraints in the MPC controller formulation. Then, an extended MPC method solved by differential evolution optimization algorithm is proposed to realize optimal smooth path following based on driving path features. Finally, simulation and real experiments are carried out to evaluate the feasibility and the effectiveness of the extended MPC scheme. Results indicate that the proposed method can obtain the smooth transition to follow the optimal drivable path and satisfy the lateral dynamic stability and environmental constraints, which can improve the path following quality for better ride comfort and road availability of autonomous vehicles.

KEYWORDS   autonomous vehicles, vehicle dynamic modeling, model predictive control, path following, optimization algorithm

1   Introduction

Autonomous vehicles have wide application potentials in intelligent transportation and military fields [1–3]. In general, they require several well-designed capabilities such as motion control, path planning and following, positioning, mapping, and decision making [4]. Path following is controlling the steering action such that the vehicle can move along the reference lane path with good driving safety and riding comfort according to the motion planning and vehicle driving state feedback. To achieve path following accuracy and driving stability simultaneously, path following control should effectively improve the optimal path following performance of autonomous vehicles under different driving conditions [5]. Interaction or integration between the vehicle and the road dynamics can be very substantial to enhancing the overall performance of path following. Many classical control approaches have been deployed in the path following of autonomous vehicles, which can be classified into four categories.

(1) Geometric and kinematic control. It is based on the geometric and kinematic vehicle model. Pure pursuit and Stanley methods are the most popular geometric controllers among the existing methods, which are developed for DARPA Grand Challenge vehicles [6–8]. These types of controllers are suitable for smooth path following at low speeds because they neglect the vehicle nonlinear dynamics that is very crucial at high speeds [9].

(2) Model-free control. No mathematical models are used, and vehicle dynamics is treated as a black box. Simple PID, fuzzy, and neural network control methods are designed for automatic steering control based on tracking errors [10–13]. Moreover, several adaptive composite control methods, such as fuzzy-PID, neural network PID, adaptive fuzzy, and neural controllers [14–16], are usually applied to perform parameter adjustment.

(3) State feedback control. The controller is designed by using accurate system models and implement the rigorous operations in the explicit control laws [2,17,18]. For instance, linear quadratic regulator, sliding mode control, and H infinity control methods are several

common state feedback control techniques, where Lyapunov theory is generally used to evaluate the nominal stability of such systems [19,20]. The said methods cannot effectively consider the vehicle and road constraints, resulting in actuator saturation or even instable dynamics.

(4) Model predictive control (MPC). It can predict the multistep output behaviors of nonlinear system dynamics in the future and correct the following error of the system by solving the constrained optimal control problem in the moving horizon [21,22]. It can also explicitly tackle the multiconstraint problem of MIMO systems under sophisticated dynamic environments. Therefore, it has been widely used in the path following of autonomous vehicles [23,24].

The key tasks of MPC include accurate dynamic modeling, multiconstraint design, and optimization solution. Taking the high-fidelity dynamic model as a predictive model can enhance the predictive ability for the future dynamic behaviors of the vehicle and ensure a good maneuverability. The kinematic model without tires and lateral dynamics is generally used in low-speed driving scenarios [25]. Most vehicle lateral dynamics is modeled by a bicycle model due to its simplicity and high practicability, which is beneficial to improving the discretization and prediction of MPC [26]. Full vehicle dynamic model is also applied to simulate the lateral and longitudinal forces generated on each wheel during maneuvering [27]. It can completely describe the nonlinear characteristics of vehicle slip and yaw but also greatly increases its computational cost.

To date, different error performance evaluation criteria have been considered in path following controllers to track lateral error, heading error, preview look-ahead distance, and sideslip angle error and their derivatives [17,28,29], which are focused on vehicle dynamics for improving the path following performance. The multiconstraint design is also required to tackle the boundary problem from the vehicle motion and driving environment under several unstable maneuver conditions. A wide range of lateral dynamic, actuator, and road environmental constraints are encountered in path following, which are imposed on the control and output variables [30–33]. Finally, the designed MPC control objective forms an online optimization problem. Furthermore, three kinds of metaheuristic optimization algorithms are presented to solve the optimization of the MPC controllers used for mobile robot path tracking control [34]. CVXGEN, particle swarm optimization, and genetic algorithm are also used in iterative operations [35–37].

However, the current path following methods of autonomous vehicles mainly focus on the lateral dynamic control, but the roll dynamics on the road bank is often overlooked. As roll motion is related to vehicle model fidelity and affects the safety and ride comfort of vehicles, roll effects should be considered in the vehicle dynamic modeling for path following problem. The road centerline derived by minimizing the lateral error and heading error is strictly tracked in most path following cases, and many control techniques have been applied to address the path planning and path following problems through two independent controllers separately [32,33,38].

Nevertheless, the reference path generated by the road centerline or path planner may not be smooth enough for or even conflicts with vehicle dynamics, which may lead to overshoot, oscillation, or even instability for autonomous vehicles following it. To solve these problems, the improved multiconstraint design and optimization solution with the integration of vehicle and road dynamics should be considered in path following operations, which are the main motivations for the research work reported in this paper. The main contributions of this paper include the following:

(1) The vehicle lateral and roll constraint design for stability and environmental envelopes is further concretely derived in MPC controller formulation.

(2) An extended MPC scheme considering the driving path features is created to tackle the interaction of vehicle and road dynamics in path following operations.

(3) The proposed scheme can obtain the smooth transition on the optimal drivable path and improve the stability and maneuverability of autonomous vehicles.

The rest of the paper is organized as follows. In Section 2, vehicle dynamic modeling for path following problems, in which road curvature and inclination are used to describe the vehicle lateral and roll dynamics accurately, is described. In Section 3, a multiconstraint MPC formulation is explicitly designed by considering sideslip and rollover envelopes, road boundaries, and actuator saturation, in which the extended MPC scheme considering driving path features is presented and differential evolution (DE) optimization algorithm is used for its solution. In Section 4, Carsim–Simulink joint simulations and hardware in the loop (HIL) test are conducted to verify the effectiveness of the proposed extended MPC path tracking method. Finally, a brief conclusion and future prospects are provided in Section 5.

2 Vehicle dynamic modeling for path following problem

Building a high-precision vehicle model is the key task to determining the overall performance of the path following controller, which requires accurately capturing the lateral and roll dynamics [39]. However, the flat road is considered in most modeling works for the path following problem, and the vehicle roll effect from the suspension system is generally ignored in most modeling works for the path following problem, which is not

conducive to the future dynamic prediction and constraint exertion under complex road and high-speed conditions. The road bank must be taken to enhance the model fidelity of the path tracking controller. Figure 1 shows the schematic diagram of vehicle dynamics. The vehicle can be reduced to a two-tire configuration at the front and the rear owing to symmetric dynamics of the left and right tracks. Considering the rollover instability of the vehicle, the dynamic features of sprung mass and unsprung mass under road inclination conditions are also discussed.

In the assumption of small angles, the differential dynamic equations can be described by

$$\begin{cases} m(\dot{v}_y + v_x r) = m_s h \ddot{\varphi} + 2F_{yf} + 2F_{yr} - mg\varphi_r, \\ I_z \dot{r} = 2F_{yf} l_f - 2F_{yr} l_r, \\ I_x \ddot{\varphi} = m_s g h(\varphi + \varphi_r) + m_s h(\dot{v}_y + v_x r - h\ddot{\varphi}) - K_\varphi \varphi - C_\varphi \dot{\varphi}, \\ \dot{e}_y = v_x e_\psi + v_y, \\ \dot{e}_\psi = r - \kappa v_x, \end{cases}$$

(1)

where m and m_s are the total vehicle mass and the sprung vehicle mass, respectively, l_f and l_r are the distances from the center of gravity of the vehicle to the front and rear axles, respectively, I_x and I_z are the roll moment of inertia and the yaw moment of inertia, respectively, K_φ and C_φ represent the combined roll stiffness coefficient and the roll damping coefficient, respectively, h is the distance from the spring mass to the roll center, r is the vehicle yaw rate, κ is the reference road curvature, v_x and v_y are the longitudinal and lateral velocities in the x and y directions, respectively, F_{yf} and F_{yr} are the lateral forces for the front and rear tires, respectively, φ and φ_r are the roll angle of the vehicle and the road bank angle, respectively, e_y and e_ψ are the lateral and heading errors of the vehicle, respectively, which are obtained by calculating the difference between road path and output vehicle trajectory, and g is the gravitational acceleration.

The nonlinear dynamics of the vehicle is mainly reflected in the lateral tire force; therefore, a reasonable linearization of the tire model is approximated based on a tire brush model, where the lateral forces of the front and rear tires are modeled as affine [40]:

$$F_{yj} = \begin{cases} C_{dj}(\alpha_j + \alpha_{hj}) - C_{0j}, & \alpha_j < -\alpha_{hj}, \\ C_j \alpha_j, & -\alpha_{hj} \leqslant \alpha_j \leqslant \alpha_{hj}, \\ C_{dj}(\alpha_j - \alpha_{hj}) + C_{0j}, & \alpha_j > \alpha_{hj}, \end{cases}$$

(2)

where $j = \{f, r\}$ represents the front and rear tires, α_j is the tire slip angle, α_{hj} is the saturation slip angle, and C_j, C_{dj}, and C_{0j} are the equivalent tire cornering stiffness identified from experimental data or more complex tire models.

The tire slip angles can also be linearized in the assumption of small angles.

$$\begin{cases} \alpha_f = \tan^{-1}\left(\dfrac{v_y + l_f r}{v_x}\right) - \delta_f = \dfrac{v_y + l_f r}{v_x} - \delta_f, \\ \alpha_r = \tan^{-1}\left(\dfrac{v_y - l_r r}{v_x}\right) = \dfrac{v_y - l_r r}{v_x}, \end{cases}$$

(3)

where δ_f is the front steer angle.

The tire forces symmetrically construct three regions of operations, namely, negative saturation, linear saturation, and positive saturation. Figure 2 shows the phase plane trajectories of the nonlinear vehicle dynamics generated by Eqs. (1)–(3) under different initial conditions. Two distinct areas with unstable and stable trajectories are plotted by red and blue marks separately. The stable operating region of the tire is determined by analyzing the lateral dynamic behaviors in the phase plane. Beside the stable equilibrium at the origin, two unstable equilibria clearly appear at approximately $(\alpha_f, \alpha_r) = \pm(0.12, 0.15)$ rad.

Let $\boldsymbol{x} = [\, v_y \quad r \quad \varphi \quad \dot{\varphi} \quad e_y \quad e_\psi \,]^T$ be the state vector, and δ_f is the control input $\boldsymbol{u}$. In addition, $\boldsymbol{\gamma} = [\varphi_r \; \kappa]^T$ is considered the external disturbance input. A constant vehicle longitudinal velocity is also assumed. As a result, the vehicle model with lateral and roll dynamics is described below:

$$\boldsymbol{M\dot{x}} = \boldsymbol{A}_m \boldsymbol{x} + \boldsymbol{B}_{um}\boldsymbol{u} + \boldsymbol{B}_{vm}\boldsymbol{\gamma},$$
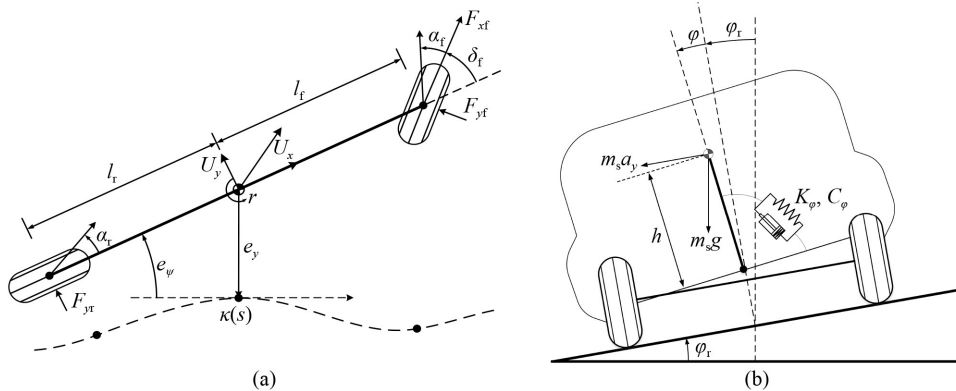
(4)

Fig. 1 Vehicle dynamic modeling with road bank: (a) lateral dynamics, (b) roll dynamics.

where M is system matrix, and

$$M = \begin{bmatrix} m & 0 & 0 & 0 & -m_s h & 0 \\ 0 & I_z & 0 & 0 & 0 & 0 \\ 0 & 0 & 1 & 0 & 0 & 0 \\ -m_s h & 0 & 0 & I_x + m_s h^2 & 0 & 0 \\ 0 & 0 & 0 & 0 & 1 & 0 \\ 0 & 0 & 0 & 0 & 0 & 1 \end{bmatrix},$$

A_m is system state matrix, B_{um} is system input matrix, and B_{vm} is system disturbance matrix.

Equation (4) can be further rewritten as

$$\dot{x} = A_c x + B_{uc} u + B_{vc} \gamma, \tag{5}$$

where A_c is state matrix, $A_c = M^{-1} A_m$, B_{uc} is input matrix, $B_{uc} = M^{-1} B_{um}$, and B_{vc} is disturbance matrix, $B_{vc} = M^{-1} B_{vm}$.

The following output map for yaw angle and lateral position states are defined.

$$y = C_c x = \begin{bmatrix} 0 & 0 & 0 & 0 & 1 & 0 \\ 0 & 0 & 0 & 0 & 0 & 1 \end{bmatrix} x, \tag{6}$$

where y is output vector, and C_c is output matrix.
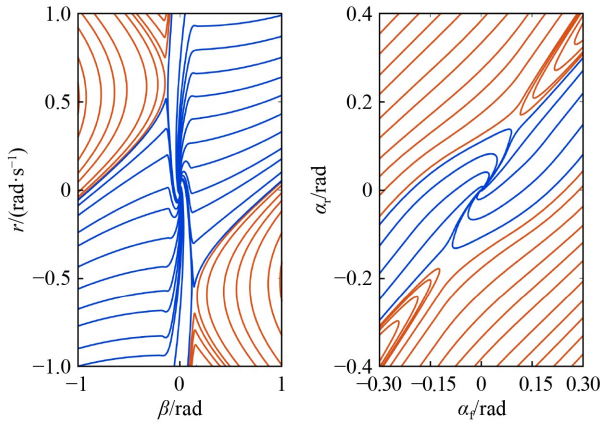

Fig. 2   Phase plane trajectories of nonlinear vehicle dynamics: (a) lateral dynamic, (b) tire slip angle.

3   Design of MPC-based path following control

In this section, combined with the vehicle model captured the lateral and roll dynamics, the MPC controller formulation with multiple constraints is first performed to deal with the prediction behavior, optimization, and constraint envelopes under the road bank and curvature disturbances. Then, an extended MPC-based control scheme considering the integration of vehicle and road dynamics is presented for the smooth path following of autonomous vehicles. Figure 3 shows a block diagram of the extended MPC-based control scheme.

3.1   MPC controller formulation

Considering the constantly changing road surface and traffic circumstances, a remarkable process in the MPC controller design for path following is to predict the future behaviors of the vehicle at each sample time T_s correspondingly. The path following problem is formulated by using a discrete-time prediction model and solved in receding horizon. Equations (5) and (6) need to be transformed into a discrete state–space model at sample time. The discrete matrices for state variables, control input, external inputs, and output variables are described by

$$\begin{cases} A_d = e^{A_c T_s}, \\ B_{ud} = \int_{kT_s}^{(k+1)T_s} e^{A_c[(k+1)T_s - \tau]} d\tau \cdot B_{uc}, \\ B_{vd} = \int_{kT_s}^{(k+1)T_s} e^{A_c[(k+1)T_s - \tau]} d\tau \cdot B_{vc}. \end{cases} \tag{7}$$

where A_d is discrete state matrix, B_{ud} is discrete input matrix, B_{vd} is discrete disturbance matrix, and k is discrete time.

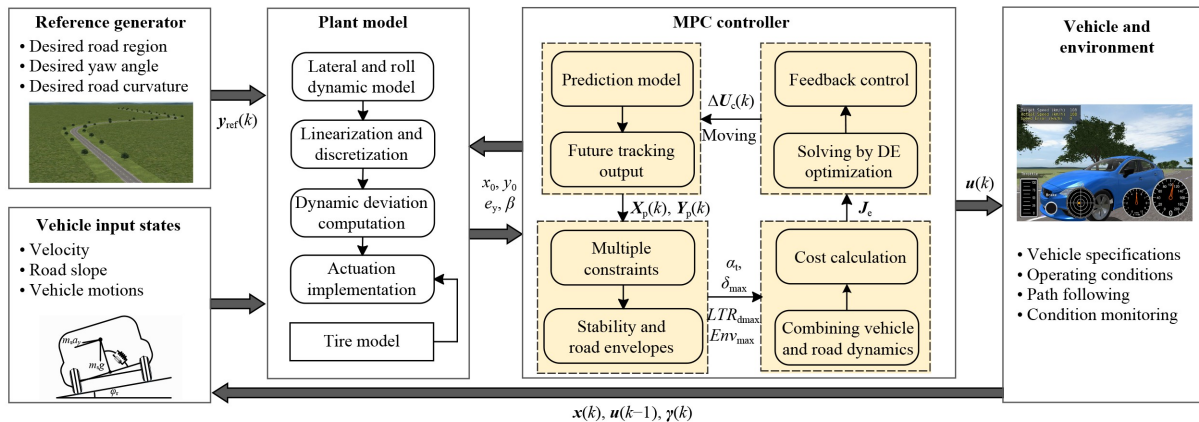Therefore, the discrete state space model is obtained as

Fig. 3   Extended MPC-based control scheme.

$$\begin{cases} \boldsymbol{x}\,(k+1) = \boldsymbol{A}_\mathrm{d}\boldsymbol{x}\,(k) + \boldsymbol{B}_\mathrm{ud}\boldsymbol{u}\,(k) + \boldsymbol{B}_\mathrm{vd}\boldsymbol{\gamma}\,(k), \\ \boldsymbol{y}\,(k) = \boldsymbol{C}_\mathrm{d}\boldsymbol{x}\,(k), \end{cases} \tag{8}$$

where $\boldsymbol{C}_\mathrm{d}$ is discrete output matrix, and $\boldsymbol{C}_\mathrm{d} = \boldsymbol{C}_\mathrm{c}$.

An integrator is introduced to reduce the control error and enhance the precise execution. The control input of the path following controller is obtained by the incremental form $\Delta \boldsymbol{u}$.

$$\begin{cases} \boldsymbol{\xi}(k+1) = \boldsymbol{A}\boldsymbol{\xi}(k) + \boldsymbol{B}_\mathrm{u}\Delta \boldsymbol{u}\,(k) + \boldsymbol{B}_\mathrm{v}\boldsymbol{\gamma}(k), \\ \boldsymbol{y}\,(k) = \boldsymbol{C}\boldsymbol{\xi}(k), \end{cases} \tag{9}$$

where augmented state vector $\boldsymbol{\xi}(k) = \begin{bmatrix} \boldsymbol{x}\,(k) \\ \boldsymbol{u}\,(k-1) \end{bmatrix}$ and input

increment $\Delta \boldsymbol{u}\,(k) = \boldsymbol{u}\,(k) - \boldsymbol{u}\,(k-1)$, $\boldsymbol{A}$ is augmented state

matrix, $\boldsymbol{A} = \begin{bmatrix} \boldsymbol{A}_\mathrm{d} & \boldsymbol{B}_\mathrm{ud} \\ \boldsymbol{0} & \boldsymbol{I} \end{bmatrix}$, $\boldsymbol{B}_\mathrm{u}$ is augmented input matrix,

$\boldsymbol{B}_\mathrm{u} = \begin{bmatrix} \boldsymbol{B}_\mathrm{ud} \\ \boldsymbol{I} \end{bmatrix}$, $\boldsymbol{B}_\mathrm{v}$ is augmented disturbance matrix,

$\boldsymbol{B}_\mathrm{v} = \begin{bmatrix} \boldsymbol{B}_\mathrm{vd} \\ \boldsymbol{0} \end{bmatrix}$, and $\boldsymbol{C}$ is augmented output matrix,

$\boldsymbol{C} = \begin{bmatrix} \boldsymbol{C}_\mathrm{d} & \boldsymbol{0} \end{bmatrix}$.

This work assumes that the prediction horizon is N_p, the control horizon is N_c ($N_\mathrm{c} < N_\mathrm{p}$), and state variable $\boldsymbol{\xi}(k)$ captures the current plant dynamic behaviors by measurement or estimation. According to the current vehicle state at time k, the future vehicle dynamics performed at times $k+1$ to $k+N_\mathrm{p}$ could be predicted by

$$\begin{cases} \boldsymbol{\xi}(k+1) = \boldsymbol{A}\boldsymbol{\xi}(k) + \boldsymbol{B}_\mathrm{u}\Delta \boldsymbol{u}\,(k) + \boldsymbol{B}_\mathrm{v}\boldsymbol{\gamma}(k), \\ \boldsymbol{\xi}(k+2) = \boldsymbol{A}^2\boldsymbol{\xi}(k) + \boldsymbol{A}\boldsymbol{B}_\mathrm{u}\Delta \boldsymbol{u}\,(k) + \boldsymbol{B}_\mathrm{u}\Delta \boldsymbol{u}\,(k+1) \\ \qquad\quad + \boldsymbol{A}\boldsymbol{B}_\mathrm{v}\boldsymbol{\gamma}(k) + \boldsymbol{B}_\mathrm{v}\boldsymbol{\gamma}(k), \\ \vdots \\ \boldsymbol{\xi}(k+N_\mathrm{c}) = \boldsymbol{A}^{N_\mathrm{c}}\boldsymbol{\xi}(k) + \boldsymbol{A}^{N_\mathrm{c}-1}\boldsymbol{B}_\mathrm{u}\Delta \boldsymbol{u}\,(k) + \cdots \\ \qquad\quad + \boldsymbol{B}_\mathrm{u}\Delta \boldsymbol{u}\,(k+N_\mathrm{c}-1) + \boldsymbol{A}^{N_\mathrm{c}-1}\boldsymbol{B}_\mathrm{v}\boldsymbol{\gamma}(k) \\ \qquad\quad + \cdots + \boldsymbol{B}_\mathrm{v}\boldsymbol{\gamma}(k), \\ \vdots \\ \boldsymbol{\xi}(k+N_\mathrm{p}) = \boldsymbol{A}^{N_\mathrm{p}}\boldsymbol{\xi}(k) + \boldsymbol{A}^{N_\mathrm{p}-1}\boldsymbol{B}_\mathrm{u}\Delta \boldsymbol{u}\,(k) + \cdots \\ \qquad\quad + \boldsymbol{A}^{N_\mathrm{p}-N_\mathrm{c}}\boldsymbol{B}_\mathrm{u}\Delta \boldsymbol{u}\,(k+N_\mathrm{c}-1) \\ \qquad\quad + \boldsymbol{A}^{N_\mathrm{p}-1}\boldsymbol{B}_\mathrm{v}\boldsymbol{\gamma}(k) + \cdots + \boldsymbol{B}_\mathrm{v}\boldsymbol{\gamma}(k), \end{cases} \tag{10}$$

where $\Delta \boldsymbol{u}(k+N_\mathrm{c}) = \Delta \boldsymbol{u}(k+N_\mathrm{c}+1) = \cdots = \Delta \boldsymbol{u}(k+N_\mathrm{p}-1) = 0$.

Control input remains constant when control horizon exceeds the N_c time steps. By using successive substitution, $\boldsymbol{u}(k+N_\mathrm{c}-1) = \boldsymbol{u}(k+N_\mathrm{c}) = \cdots = \boldsymbol{u}(k+N_\mathrm{p}-1)$ is assumed. In this case, the output states at times $k+1$ to $k+N_\mathrm{p}$ could be computed by combining Eqs. (8)–(10).

$$\boldsymbol{y}\,(k+i) = \boldsymbol{C}\boldsymbol{\xi}(k+i), \quad i = 1, 2, ..., N_\mathrm{p}. \tag{11}$$

Furthermore, the predicted sequences over a horizon N_p and control sequences over a horizon N_c are defined as

$$\boldsymbol{X}_\mathrm{p}(k) = \begin{bmatrix} \boldsymbol{\xi}(k+1) \\ \boldsymbol{\xi}(k+2) \\ \vdots \\ \boldsymbol{\xi}(k+N_\mathrm{p}) \end{bmatrix},$$

$$\boldsymbol{Y}_\mathrm{p}(k) = \begin{bmatrix} \boldsymbol{y}\,(k+1) \\ \boldsymbol{y}\,(k+2) \\ \vdots \\ \boldsymbol{y}\,(k+N_\mathrm{p}) \end{bmatrix},$$

$$\Delta \boldsymbol{U}_\mathrm{c}(k) = \begin{bmatrix} \Delta \boldsymbol{u}\,(k) \\ \Delta \boldsymbol{u}\,(k+1) \\ \vdots \\ \Delta \boldsymbol{u}\,(k+N_\mathrm{c}-1) \end{bmatrix}, \tag{12}$$

where $\boldsymbol{X}_\mathrm{p}(k)$ is N_p-step state prediction at time k, $\boldsymbol{Y}_\mathrm{p}(k)$ is N_p-step output prediction at time k, and $\Delta \boldsymbol{U}_\mathrm{c}(k)$ is N_c-step input variations at time k.

By combining Eqs. (11) and (12), the predicted state and output vector is computed as

$$\begin{cases} \boldsymbol{X}_\mathrm{p}(k) = \tilde{\boldsymbol{A}}_x\boldsymbol{\xi}(k) + \tilde{\boldsymbol{B}}_{\mathrm{ux}}\Delta \boldsymbol{U}_\mathrm{c}(k) + \tilde{\boldsymbol{B}}_{\mathrm{vx}}\boldsymbol{\gamma}(k), \\ \boldsymbol{Y}_\mathrm{p}(k) = \tilde{\boldsymbol{A}}\boldsymbol{\xi}(k) + \tilde{\boldsymbol{B}}_\mathrm{u}\Delta \boldsymbol{U}_\mathrm{c}(k) + \tilde{\boldsymbol{B}}_\mathrm{v}\boldsymbol{\gamma}(k), \end{cases} \tag{13}$$

where $\tilde{\boldsymbol{A}}_x$, $\tilde{\boldsymbol{B}}_{\mathrm{ux}}$, and $\tilde{\boldsymbol{B}}_{\mathrm{vx}}$ are the predicted state matrix, input matrix, and disturbance matrix, respectively, and $\tilde{\boldsymbol{A}}$, $\tilde{\boldsymbol{B}}_\mathrm{u}$, and $\tilde{\boldsymbol{B}}_\mathrm{v}$ are the predicted state matrix, input matrix, and disturbance matrix for output system, respectively.

Equation (13) shows the prediction function, in which the future output trajectories of the model are predicted by using current state $\boldsymbol{\xi}(k)$, input variations $\Delta \boldsymbol{U}_\mathrm{c}(k)$, and external disturbance input $\boldsymbol{\gamma}(k)$.

The control sequence can be obtained by solving the optimization objective. The goal of autonomous vehicle lateral control is to track the desired road centerline accurately in the existing research [30,38], and conventional cost function $\boldsymbol{J}_\mathrm{c}$ applied to the above prediction model is generally selected as

$$\boldsymbol{J}_\mathrm{c} = \sum_{i=1}^{N_\mathrm{p}} \left\| \boldsymbol{y}\,(k+i) - \boldsymbol{y}_\mathrm{ref}\,(k+i) \right\|_Q^2 + \sum_{i=0}^{N_\mathrm{c}-1} \left\| \Delta \boldsymbol{u}\,(k+i) \right\|_R^2 + \lambda\varepsilon^2, \tag{14}$$

where $\boldsymbol{y}_\mathrm{ref}(k+i)$ is the desired reference output, ε is a slack variable, $\boldsymbol{Q}$ and $\boldsymbol{R}$ are the corresponding output and input weight matrices, λ is slack weight, and the large weights will provide a more important priority to perform the corresponding optimization objective. The first term describes the predictive error between the prediction and reference outputs. The second term is the appropriate control inputs for the steering system. The third item reflects the optimal relaxation ability of the system, which avoids the infeasibility solution.

By substituting predicted output Eq. (13) into cost function Eq. (14), a quadratic expression in terms of the input variations $\Delta \boldsymbol{U}_\mathrm{c}(k)$ can be obtained by

$$\boldsymbol{J}_\mathrm{c} = \boldsymbol{V}_k^\mathrm{T}\boldsymbol{H}_k\boldsymbol{V}_k + \boldsymbol{G}_k\boldsymbol{V}_k + \boldsymbol{P}_k, \tag{15}$$

where H_k, V_k, G_k, and P_k are quadratic transformation matrices that converts Eq. (14) into Eq. (15).

The output deviation $E(k)$ of the free response system in the predictive domain is equivalently arranged into

$$E(k) = \tilde{A}\xi(k) + \tilde{B}_v\gamma(k) - Y_{ref}(k), \qquad (16)$$

where Y_{ref} is reference output matrix.

Considering the limited work conditions encountered in the control input, control increment, and predictive output at each time step, the path following problem is enforced to satisfy the following control constraints, which are concretely described in multiconstraint design.

$$\begin{cases} \Delta u_{min}(k+i) \leqslant \Delta u(k+i) \leqslant \Delta u_{max}(k+i), & i = 0, 1, ..., N_c - 1, \\ u_{min}(k+i) \leqslant u(k+i) \leqslant u_{max}(k+i), & i = 0, 1, ..., N_c - 1, \\ y_{min}(k+i) \leqslant y(k+i) \leqslant y_{max}(k+i), & i = 1, 2, ..., N_p, \end{cases} \qquad (17)$$

where Δu_{min} and Δu_{max} are minimum and maximum of input increment, respectively, u_{min} and u_{max} are minimum and maximum of control input, respectively, and y_{min} and y_{max} are minimum and maximum of output vector, respectively.

To solve the control increment of the objective function in the moving control horizons, the following optimization problem is performed by

$$\min_{\Delta U_c, \varepsilon} \quad J_c(\xi(k), u(k), \Delta U_c(k), \varepsilon),$$
$$\text{s.t.} \quad C_1\Delta\delta_{fmin} \leqslant \Delta U_c(k) \leqslant C_1\Delta\delta_{fmax},$$
$$C_1\delta_{fmin} \leqslant C_1 u(k-1) + C_2\Delta U_c(k) \leqslant C_1\delta_{fmax},$$
$$C_3 y_{hmin} \leqslant \tilde{A}_h\xi(k) + \tilde{B}_{uh}\Delta U_c(k) + \tilde{B}_{vh}\gamma(k) \leqslant C_3 y_{hmax},$$
$$C_4 y_{smin} - \varepsilon \leqslant \tilde{A}_s\xi(k) + \tilde{B}_{us}\Delta U_c(k) + \tilde{B}_{vs}\gamma(k) \leqslant$$
$$C_4 y_{smax} + \varepsilon, \qquad (18)$$

where $C_1 = \begin{bmatrix} 1 \\ 1 \\ \vdots \\ \vdots \\ 1 \end{bmatrix}_{N_c \times 1}$, $C_2 = \begin{bmatrix} 1 & 0 & \cdots & 0 \\ 1 & 1 & \cdots & 0 \\ \vdots & \vdots & \ddots & \vdots \\ 1 & 1 & \cdots & 1 \end{bmatrix}_{N_c \times N_c}$, $C_3 = $

$\begin{bmatrix} I_{N_{yh}} \\ I_{N_{yh}} \\ \vdots \\ I_{N_{yh}} \end{bmatrix}_{N_p \times 1}$, $C_4 = \begin{bmatrix} I_{N_{ys}} \\ I_{N_{ys}} \\ \vdots \\ I_{N_{ys}} \end{bmatrix}_{N_p \times 1}$, δ_{fmin} and δ_{fmax} are the minimum

andmaximum of steer angle in the steering actuator, $\Delta\delta_{fmin}$ and $\Delta\delta_{fmax}$ are the minimum and maximum of steer angle increment, y_{hmin} and y_{hmax} are the lower and upper bounds on the output variables to be hard constrained, y_{smin} and y_{smax} are the lower and upper bounds on the output variables to be soft constrained, $\tilde{A}_h$, $\tilde{B}_{uh}$, and $\tilde{B}_{vh}$ are coefficient matrices for hard constraints, and $\tilde{A}_s$, $\tilde{B}_{us}$, and $\tilde{B}_{vs}$ are coefficient matrices for soft constraints, which can be computed by the defined multiple constraints.

The generated optimization problem consisting of input variations $\Delta U_c(k)$ and the linear constraints can be solved by

$$\min_{\Delta U_c, \varepsilon} \begin{bmatrix} \Delta U_c(k) \\ \varepsilon \end{bmatrix}^T H_k \begin{bmatrix} \Delta U_c(k) \\ \varepsilon \end{bmatrix} + G_k \begin{bmatrix} \Delta U_c(k) \\ \varepsilon \end{bmatrix},$$
$$\text{s.t.} \quad \begin{bmatrix} C_1\Delta\delta_{fmin} \\ 0 \end{bmatrix} \leqslant \begin{bmatrix} \Delta U_c(k) \\ \varepsilon \end{bmatrix} \leqslant \begin{bmatrix} C_1\Delta\delta_{fmax} \\ M \end{bmatrix},$$
$$\begin{bmatrix} C_2 & 0 \\ -C_2 & 0 \\ \tilde{B}_{uh} & 0 \\ -\tilde{B}_{uh} & 0 \\ \tilde{B}_{us} & -1 \\ -\tilde{B}_{us} & -1 \end{bmatrix} \begin{bmatrix} \Delta U_c(k) \\ \varepsilon \end{bmatrix} \leqslant$$
$$\begin{bmatrix} C_1\delta_{fmax} - C_1 u(k-1) \\ -C_1\delta_{fmax} + C_1 u(k-1) \\ C_3 y_{hmax} - \tilde{A}_h\xi(k) - \tilde{B}_{vh}\gamma(k) \\ -C_3 y_{hmin} + \tilde{A}_h\xi(k) + \tilde{B}_{vh}\gamma(k) \\ C_4 y_{smax} - \tilde{A}_s\xi(k) - \tilde{B}_{vs}\gamma(k) \\ -C_4 y_{smin} + \tilde{A}_s\xi(k) + \tilde{B}_{vs}\gamma(k) \end{bmatrix}. \qquad (19)$$

3.2 Multiconstraint design for stability and environmental envelopes

Stability and environmental envelopes in the above optimization problem are further given by the multiconstraint design. Given that an excessively large tire sideslip angle will emerge the vehicle slip instability shown in Fig. 2, the tire slip angle imposes a limit angle α_t within the stable region to avoid vehicle slip and ensure the effectiveness of the linearized tire model. Vehicle slip is generally characterized by the envelopes of the lateral velocity and the yaw rate, which can be derived from the saturation of the rear tires [35]. Therefore, the rear tire sideslip angle must satisfy the following constraint by combining Eq. (3).

$$\left| \frac{v_y - l_r r}{v_x} \right| \leqslant \alpha_t. \qquad (20)$$

An additional bound on yaw rate provides the maximum steady-state condition of Eq. (1), and this requires the yaw rate to yield

$$\left| r + \frac{g}{v_x}\varphi_r \right| \leqslant \min\left(\frac{C_f\alpha_t(1 + l_f/l_r)}{mv_x}, \frac{C_r\alpha_t(1 + l_r/l_f)}{mv_x} \right) = R. \quad (21)$$

To couple the constraint Eqs. (20) and (21) with the optimization problem, it is rewritten as

$$|E_1\xi(k) + F_1\gamma(k)| \leqslant M_1, \qquad (22)$$

where $E_1 = \begin{bmatrix} \frac{1}{v_x} & -\frac{l_r}{v_x} & 0 & 0 & 0 & 0 \\ 0 & 1 & 0 & 0 & 0 & 0 \end{bmatrix}$, $F_1 = \begin{bmatrix} 0 & 0 \\ \frac{g}{v_x} & 0 \end{bmatrix}$,

and $M_1 = \begin{bmatrix} \alpha_t \\ R \end{bmatrix}$.

Equation (22) can ensure that the vehicle meets the slip constraint and allow the sideslip angle to enter the nonlinear region for a short time to reduce vehicle instability. Moreover, producing a large lateral acceleration in high-speed emergency obstacle avoidance

is easy, resulting in vehicle rollover. Thus, the rollover stability of the vehicle should also be considered in lateral motion control. Lateral load transfer rate (LTR) is a widely used rollover index that can dynamically represent tire grounding force and lateral motion states, and rollover warning and active safety control based the LTR are generally used in anti rollover control [41]. However, conducting emergency control when the vehicle is about to roll over is often very late. Considering the critical unstable dynamics of high-speed vehicles, a rollover constraint is applied to prevent rollover risk, and the rollover threshold is limited within a suitable range to prevent the tires from rolling off the ground. Estimating LTR is very difficult because normal force sensors are expensive. It is difficult to be accurately captured in the complex road surface. An alternative equivalent expression for LTR, which depends on the roll states and the vehicle parameters, can be obtained by

$$LTR_d = \frac{2}{T_r}\left[\frac{m_s g h(\varphi + \varphi_r) + m_s h(\dot{v}_y + v_x r - h\ddot{\varphi}) - I_x \ddot{\varphi}}{mg}\right],$$
(23)

where LTR_d is the equivalent LTR, and T_r is the vehicle track.

To prevent rollover hazard, the rollover characterization index is constrained by

$$-LTR_{dmax} \leqslant LTR_d \leqslant LTR_{dmax},$$
(24)

where LTR_{dmax} is the maximum of LTR_d.

Using the state space model, the rollover constraint matrix is expressed as

$$\left|E_2 \xi(k) + E_{d2}\dot{\xi}(k) + F_2 \gamma(k)\right| \leqslant M_2,$$
(25)

where $E_2 = \begin{bmatrix} 0 & \dfrac{2m_s h v_x}{T_r mg} & \dfrac{2m_s h}{T_r m} & 0 & 0 & 0 \end{bmatrix}$, $E_{d2} = \begin{bmatrix} \dfrac{2m_s h}{T_r mg} & 0 & 0 & \dfrac{-m_s h^2 - I_x}{T_r mg} & 0 & 0 \end{bmatrix}$, $F_2 = \begin{bmatrix} 0 & 0 \\ \dfrac{2m_s h}{T_r m} & 0 \end{bmatrix}$,

and $M_2 = LTR_{dmax}$.

Considering the obstacles and the road boundary, a collision-free optimal trajectory should be generated in a given feasible driving area. According to the envelope dimension of the vehicle and the drivable road region in the path following problem, lateral road environment envelopes on vehicle trajectory can expressed as a combination of the lateral deviation thresholds at current time k, which is represented as time-varying constraints on e_y.

$$\begin{cases} e_{yl}^k = e_{ymax}^k - \dfrac{1}{2}w - d_s, \\ e_{yr}^k = e_{ymin}^k + \dfrac{1}{2}w + d_s, \end{cases}$$
(26)

where e_{yl} represents the left road boundary, e_{yr} represents the right road boundary, w is the vehicle width, and d_s is the desired minimum distance for the vehicle to an

obstacle or road edge.

Further considering the vehicle length for feasible longitudinal road region, the vehicle envelope constraint is represented by the lateral position of the front and rear axles, which should satisfy the following conditions [30].

$$\begin{cases} y_F = y_0 + l_f(\psi + \beta), \\ y_R = y_0 - l_r(\psi + \beta), \end{cases}$$
(27)

where y_F and y_R are the lateral position of the front and rear axles, respectively, y_0 is the lateral position of the vehicle origin, ψ is the yaw angle, and β is the vehicle sideslip angle.

By combining Eqs. (26) and (27), the feasible road region obtained from the lateral and longitudinal vehicle envelopes is given by

$$Env_{min} \leqslant e_y^k \leqslant Env_{max},$$
(28)

where Env_{min} and Env_{max} are minimum and maximum feasible road regions, and $Env_{min} = \max\left(e_{yr}^k - l_f(\psi + \beta), e_{yr}^k + l_r(\psi + \beta)\right)$ and $Env_{max} = \min\left(e_{yl}^k - l_f(\psi + \beta), e_{yl}^k + l_r(\psi + \beta)\right)$.

3.3 Extended model predictive steering control scheme

The conventional MPC controller with quadratic programming cannot solve the complicated path following optimization problem, which considerably limits the flexible application of MPC. To solve this problem, an extended MPC scheme is proposed here for the smooth steering control of autonomous vehicles. Considering stability and comfort in the control process, three indictors are deployed to generate a smooth path following performance:

(1) Shortest tracking path: The path length is as small as possible, which is conducive to save driving time and fuel consumption.

(2) Minimum curvature: It requires optimal path smoothness to avoid the occurrence of dangerous conditions caused by transient large curvature path.

(3) Path heading following: It makes the tracked path heading consistent with the road centerline to reduce path deviation. Thus, the optimized cost function J_e is designed by

$$J_e = \sum_{i=1}^{N_p-1}\|\Gamma_\kappa \rho(k+i)\|^2 + \sum_{i=1}^{N_p-1}\|\Gamma_s S(k+i)\|^2$$
$$+ \sum_{i=1}^{N_p-1}\|\Gamma_\psi e_\psi(k+i)\|^2 + \sum_{i=0}^{N_c-1}\|\Gamma_u \Delta u(k+i)\|^2,$$
(29)

where $\rho(k+i)$ is the driving path curvature of the N_p-step at current time k, $S(k+i)$ is the driving path length of the N_p-step at current time k, and Γ_κ, Γ_s, Γ_ψ, and Γ_u are the corresponding weight factors.

Given the global vehicle pose (x_0, y_0, t_s) as transient variables in the time step, the corresponding path

curvature and length in the prediction step can be solved analytically by the prediction model Eq. (13). The global vehicle pose is added as

$$
\begin{cases}
\dot{y}_0 = v_x \sin\psi + v_y \cos\psi, \\
\dot{x}_0 = v_x \cos\psi - v_y \sin\psi.
\end{cases} \tag{30}
$$

To enhance the road environment envelope in the optimized cost for drivable road region, the constraint Eq. (28) is converted into a penalty function $J(Env)$ of feasible road region in this paper.

$$
J(Env) = \sum_{i=1}^{N_p-1} \left\{ \left\| \min\left(e_y^{k+i} - Env_{\min}, 0\right) \right\|^2 \right.
$$
$$
\left. + \left\| \max\left(e_y^{k+i} - Env_{\max}, 0\right) \right\|^2 \right\}. \tag{31}
$$

Combined with Eqs. (8)–(13) and (20)–(31), a new prediction model (A_p, B_p, C_p, D_p) is formed, and the extended path following optimization problem can be described as

$$
\min_{\Delta U_c(k)} J_e + \sigma J(Env), \tag{32}
$$

subject to corresponding constraint Eqs. (20)–(28) and

$$
\xi_p(k+1) = A_p \xi_p(k) + B_{up}\Delta u(k) + B_{vp}\gamma(k), \tag{33}
$$

$$
\rho(k+i) = \frac{\dot{x}_0(k+i)\ddot{y}_0(k+i) - \dot{y}_0(k+i)\ddot{x}_0(k+i)}{\left[(\dot{x}_0(k+i))^2 + (\dot{y}_0(k+i))^2\right]^{\frac{3}{2}}}, \tag{34}
$$

$$
S(k+i) = \sqrt{\left\| \Delta x(k+i) \right\|^2 + \left\| \Delta y(k+i) \right\|^2}, \tag{35}
$$

$$
e_\psi(k+i) = \psi(k+i) - \psi_{ref}(k+i), \tag{36}
$$

where σ is penalty factor, Δx and Δy are the distance between two adjacent points in x and y directions, and ψ_{ref} is the reference heading angle.

The integration and multiple constraints of vehicle and road dynamics makes the path following problem extend the derivation of intermediate variables and further non convex. To implement the extended MPC controller of path following for iteratively searching the large spaces of candidate solutions, a DE algorithm with strong robustness is used to solve the path following optimization problem, which is suitable for accelerating execution time. DE algorithm can iteratively process the constrained optimization problem by mutation, crossover, and selection operations [42]. Figure 4 describes the optimization procedure of DE algorithm in path following, and the detailed process is given as follows.

Step 1. The control increment for the front wheel steering angle is described as an encoding particle, and the initial population of control increments is randomly generated within the restrained range. In this operation, several parameters are configured, including population size, mutation weight, and crossover probability. The population is randomly initialized by

$$
\{ W_i | \Delta\delta_{fij} = \Delta\delta_{fmin} + rand \times (\Delta\delta_{fmax} - \Delta\delta_{fmin}) \},
$$
$$
(i = 1, 2, ..., P; j = 1, 2, ..., D), \tag{37}
$$

where W_i is the initial population, $\Delta\delta_{fij}$ is the initial individual, $rand$ is a random number with a uniform probability distribution in $[0, 1]$, P is the population size, and D is the number of the objective control inputs, which are generated for each control horizon in the optimization problem, that is, $D = N_c$.

Step 2. The optimization problem defined in Eq. (32) with multiple constraints is regarded as the major fitness function. As mentioned, the path curvature, length, and heading error in the prediction horizon can be calculated by using the obtained initialized population in the control step. The objective fitness function value corresponding to every reshaped population is recorded.

Step 3. A differential variable is generated by subtracting two different random objective control inputs. Mutation and crossover operations are conducted to generate new experimental input individuals in the search space by updating the differential variables. Furthermore, self-adaptive robust operations are considered in this process. For each objective control input vector, the corresponding differential mutation is expressed by

$$
V_i^{G+1} = W_{r1}^G + \eta_r \left(W_{r2}^G - W_{r3}^G\right), \tag{38}
$$

where V_i^{G+1} is the $(G+1)$th-generation mutation control inputs, the individual serial numbers r_1, r_2, and r_3 are different and randomly generated, and η_r is a robust mutation factor.

To enhance the diversity of the population, a crossover operation between initial individual $\Delta\delta_{fij}$ and its mutation v_{ij} is also performed as follows:

$$
u_{ij}^{G+1} = \begin{cases} v_{ij}^{G+1}, & \text{if rand} \leqslant CR \text{ or } j = rd, \\ \Delta\delta_{fij}^G, & \text{otherwise,} \end{cases} \tag{39}
$$

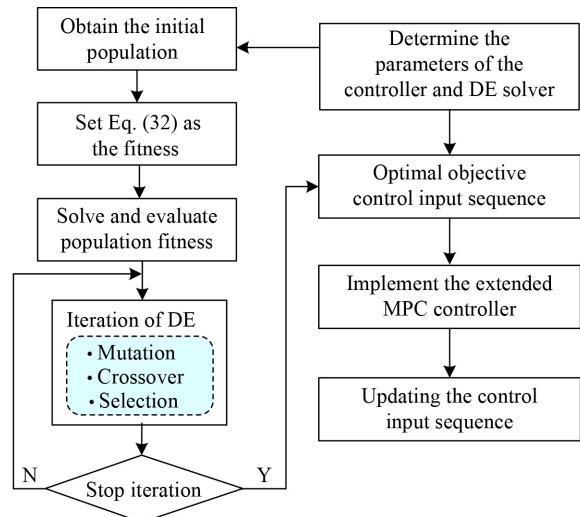where u_{ij} is the new experimental input individual, CR is

Fig. 4 Optimization procedure of DE algorithm in path following.

the crossover probability within [0, 1], and *rd* is a randomly generated integral number in [1, 2, ..., *D*].

Step 4. The fitness of each control input in the updated population is evaluated. The experimental control input sequence U_i is selected as the offspring when its fitness value is better than that of the objective input individual. Otherwise, the objective input individual remaining becomes the offspring. The evolution is repeated for a fixed iteration or ended when the search converges with a given accuracy. The best input individual is used to work out the optimization problem. The selection method is

$$W_i^{G+1} = \begin{cases} U_i^{G+1}, & \text{if } f(U_i^{G+1}) < f(W_i^G), \\ W_i^G, & \text{otherwise,} \end{cases} \tag{40}$$

where *f* is the fitness function defined in Eq. (32).

Step 5. The solved MPC controller is implemented with the first control input of the generated optimal objective sequence under the constraints. Then, the optimization problem is solved forwardly by updating these control input sequences.

---

4 Experimental results and analysis

To validate the feasibility and the effectiveness of the developed extended MPC controller for path following of autonomous vehicles, Carsim–Simulink cosimulation and HIL test are performed under different driving conditions. The parameters characterizing the vehicle dynamic model are listed as below:

m = 1530 kg,
m_s = 1370 kg,
I_x = 671.3 kg·m^2,
I_z = 2315.3 kg·m^2,
l_f = 1.11 m,
l_r = 1.67 m,
h = 0.52 m,
T_r = 1.55 m,
K_φ = 183791 N·m/rad,
C_φ = 4904 N·m·s/rad,
C_f = 66800 N/rad,

C_r = 62700 N/rad.

The main parameters used in the MPC controller by trial adjustment are shown as below:

T_s = 0.02 s,
N_p = 20,
N_c = 5,
δ_{min} = –0.52 rad,
δ_{max} = 0.52 rad,
$\Delta\delta_{min}$ = –0.12 rad/s,
$\Delta\delta_{max}$ = 0.12 rad/s,
e_{ymin} = –3 m,
e_{ymax} = 3 m,
α_t = 0.1 rad,
LTR_{dmax} = 0.7,
Γ_κ = 1500,
Γ_s = 20,
Γ_ψ= 350,
Γ_u = 250.

4.1 Simulation results

In the simulation test, the nominal path and the road surface are presented in Fig. 5, which shows the road curvature, heading, and road elevation in the path station. To verify the accuracy of rollover index LTR_d, LTR is used as nominal reference object. Figure 6 presents a comparison of LTR, LTR_d, and LTR_d without considering φ_r at the speed of 30 m/s, which clearly shows an evident error in LTR_d without considering φ_r. As the rollover index LTR_d can effectively capture LTR, it can be effectively used to characterize the rollover dynamics of the vehicle and further exert its constraint.

Figure 7 presents the simulation results of path following for considering multiple constraints and road surface in the conventional MPC controller, where the road centerline is considered the expected trajectory. More specifically, Fig. 7(a) shows that the controller with multiple constraints can effectively track the nominal path, and the path following controller with multiple constraints and road surface can remarkably further reduce tracking error. The controller without multiple constraints fails to follow the drivable path after
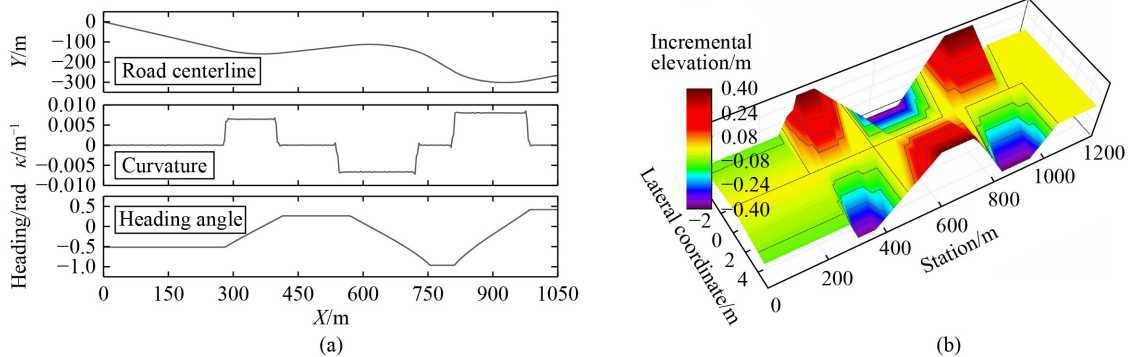

Fig. 5 Nominal path and road bank: (a) nominal path, (b) road bank.

approximately 28 s. Figure 7(b) shows that yaw angle following performs well on the controller with multiple constraints. Moreover, Fig. 7(c) shows that the lateral stability can effectively avoid the occurrence of unstable sideslip behavior in three turns. The apparent oscillating steering angle appears in Fig. 7(d) due to unstable road dynamics and mismatched trace path. To eliminate the overshoots of the conventional MPC controller, smooth path following is further considered in the proposed extended MPC controller.

Table 1 summarizes the root mean square (RMS) and maximum (Max) values of path following for conventional MPC controller. The controller considering constraints and road surface achieves smaller RMS and Max values of path following than other controllers, and its maximum yaw error and lateral velocity are reduced by 82.9% and 43.8%, respectively, compared with the
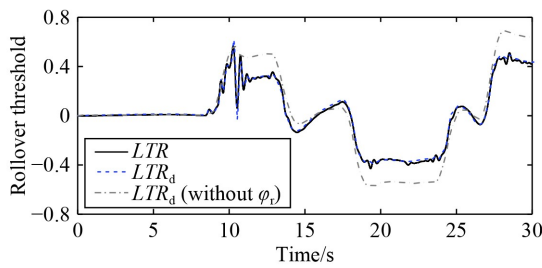
unconstrained one. Owing to the failure path following behavior shown in the unconstrained controller, its lateral error and steer angle are also far beyond the feasible tracking area.

Figure 8 presents a comparison of the simulation results of path following for conventional and extended MPC controllers at 20 m/s, where road boundary is the enveloped region by the left and right road boundaries e_{yl} and e_{yr} in Eq. (26). Although the conventional MPC controller can make it track the reference road centerline, the steering angle and the path curvature show more prominent oscillations than that of the extended MPC controller when the vehicle is turning because the road dynamic information is not considered in the conventional MPC controller, which will scarify the comfort and the stability of the vehicle. The autonomous vehicle ignores road trafficability by tracking the lane center line and is not available for the driver's driving habits. To improve the quality of path following, the driving path information of the vehicle should be considered in the path following optimization problem.

More specifically, Fig. 8(a) shows that the vehicle's driving path is constantly adjusted in the drivable road region instead of strictly tracking the road center line. The MPC controller drives the vehicle to perform the optimal transition steering behavior when the vehicle is making a turn and keep heading straight following the driving deviation from the lane center line at the end of the turn, which can preferably complete the transition steering of

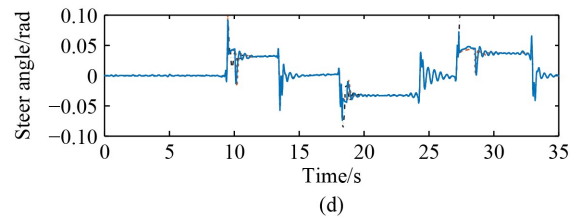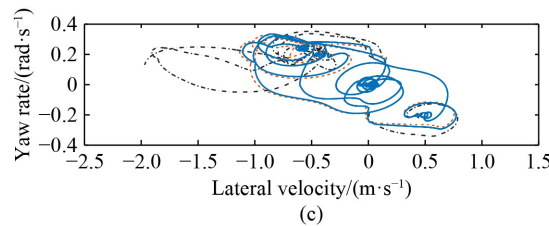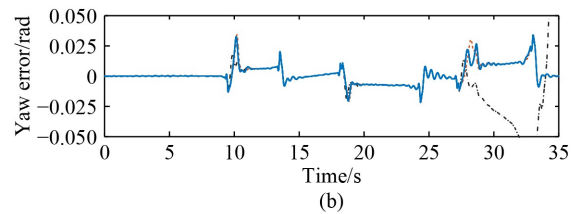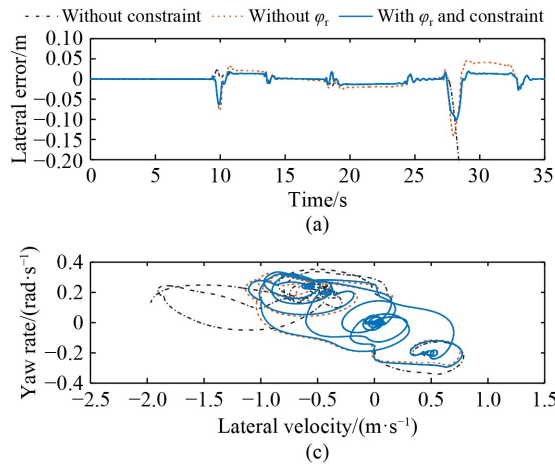**Fig. 6**   Comparison of *LTR*, *LTR*$_d$, and *LTR*$_d$ without considering φ_r.

Fig. 7   Simulation results of path following for considering multiple constraints and road bank: (a) lateral error, (b) yaw error, (c) lateral velocity versus yaw rate, and (d) steer angle.

Table 1   RMS and Max values of path following for conventional MPC controller

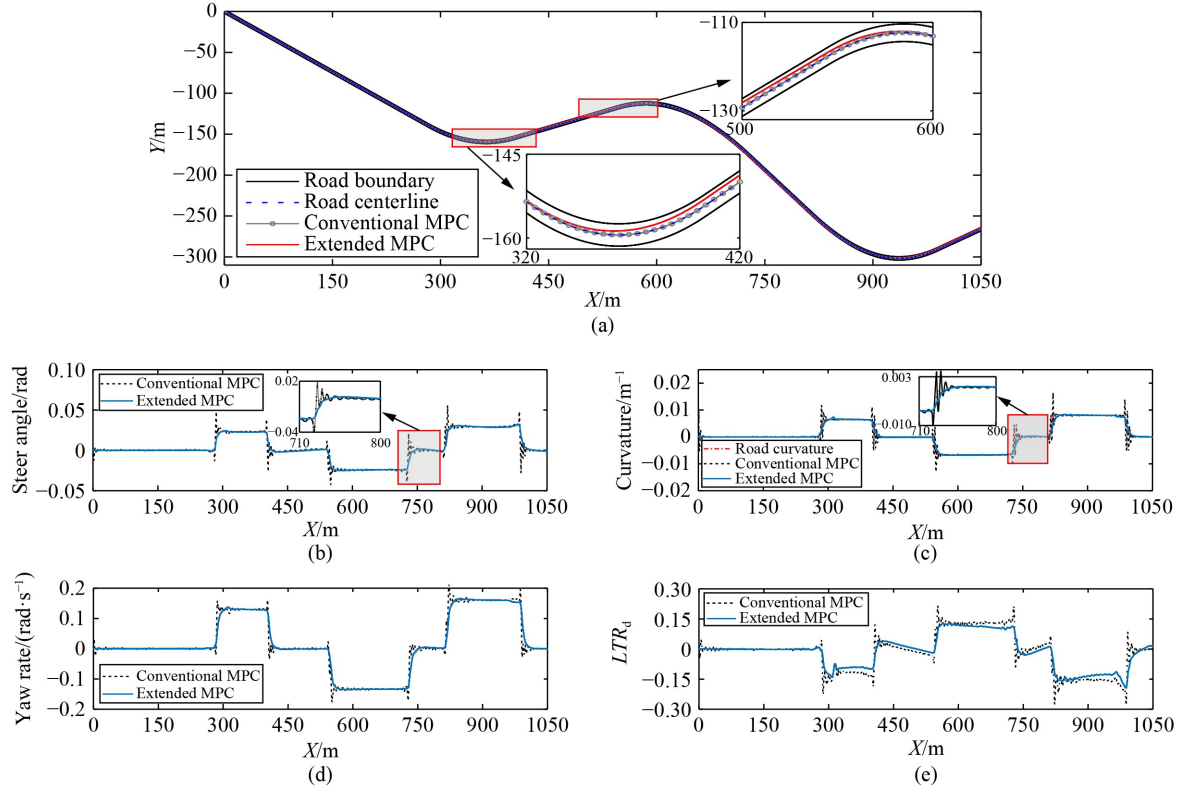| Controller	Lateral error/m		Yaw error/rad		Yaw rate/(rad·s⁻¹)		Lateral velocity/(m·s⁻¹)		Steer angle/rad	
	RMS	Max	RMS	Max	RMS	Max	RMS	Max	RMS	Max
With φ_r and constraint	0.0170	0.1019	0.0078	0.0340	0.1487	0.3347	0.3688	1.1068	0.0245	0.0915
Without φ_r	0.0249	0.1415	0.0080	0.0356	0.1498	0.3262	0.3707	1.1351	0.0247	0.1001
Without constraint	−	−	0.0283	0.1990	0.1672	0.3529	0.4438	1.9691	−	−

Fig. 8 Simulation results of path following for conventional and extended MPC controllers at 20 m/s: (a) path following, (b) steer angle, (c) path curvature, (d) yaw rate, and (e) rollover threshold.

the next turning.

Figures 8(b) and 8(c) show that the steering and curvature profiles for the extended MPC controllers are much smoother than the ones for the conventional MPC controller, especially at road corners. Its curvature is remarkably improved compared with the original one, which achieves the flexible smooth path following. In Figs. 8(d) and 8(e), the path following of the extended MPC has a higher stable yaw rate and a smaller rollover threshold than those of the conventional MPC, which can satisfy the better yaw stability and antirollover performance. Consequently, the extended MPC scheme can make full use of vehicle maneuverability and provide a more satisfactory path following performance than the conventional one.

Figure 9 shows the comparisons of the path following results for conventional and extended MPC controllers at 30 m/s. The steering performance of both schemes deteriorate at different degrees. Such situations may occur due to poor lateral stability and more sensitive steering at high-speed corners. The extended MPC scheme can achieve the acceptable path following performance and provide more superior path curvature and stable lateral dynamics. Figure 9(a) shows that the large transition steering behavior is required at high speed, which results in an increase in the steering angle performed by the autonomous vehicle, as displayed in Fig. 9(b). These results further confirm that the extended MPC controller

can ensure the good effectiveness and the robustness of smooth path following for autonomous vehicles.

The RMS and Max values of path following for conventional and extended MPC controllers under different speeds are illustrated in Table 2. The extended MPC controller can effectively reduce the RMS and Max values of path following. The RMS values of the extended MPC controller are slightly reduced compared with the traditional one, whereas its Max values show a substantial reduction. This result is not unexpected because the extended controller plays a major role in suppressing the undesirable oscillation for path following. According to the maximum steering angle and path curvature, the smoothness of the extended controller is improved by more than 40% than that of the traditional one, and its lateral stability represented by yaw rate and LTR_d is improved by approximately 19% on average.

4.2 HIL experimental results

For further verifying the performance of the proposed extended MPC scheme, an HIL test experiment based on Simulink and dSPACE system is carried out, as shown in Fig. 10. It mainly consists of the dSPACE system, steering system with servo motor, loading cylinder, sensors, monitor, and power supply. In this system, the hardware bench system realizes the real-time steering control of the autonomous vehicle and feedback of the sensor measurement data, and the loading cylinder is used
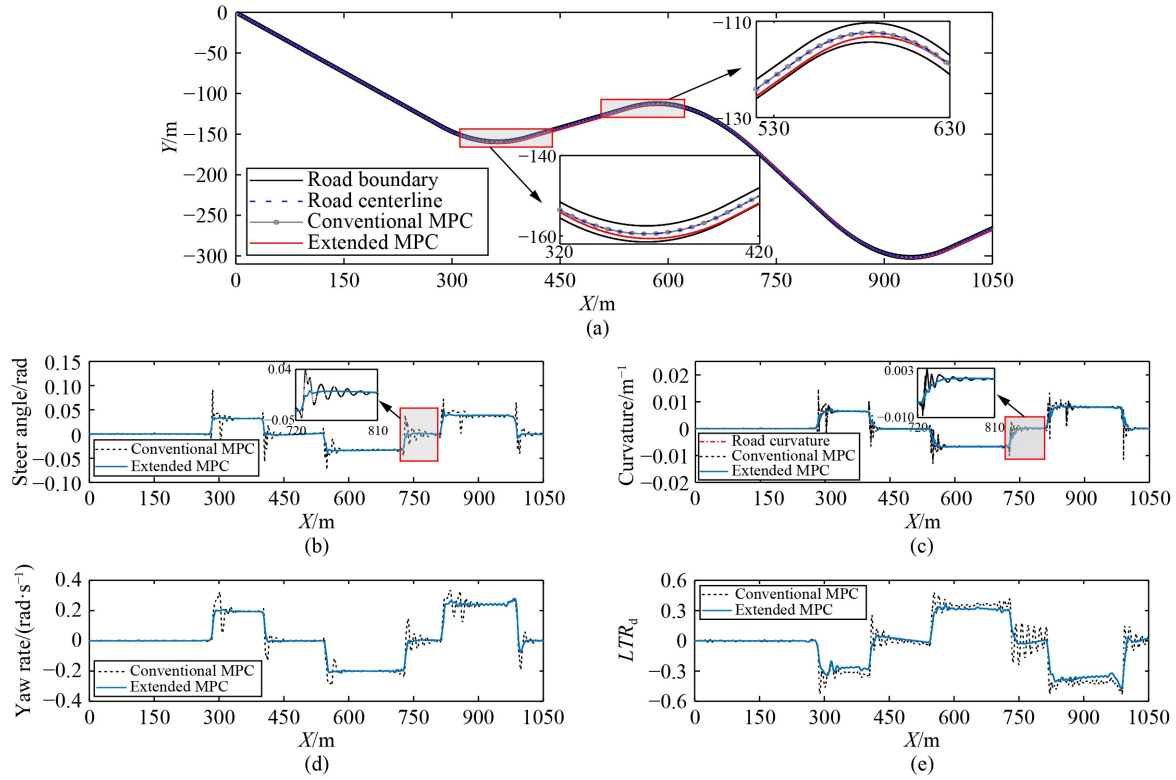
Fig. 9 Simulation results of path following for conventional and extended MPC controllers at 30 m/s: (a) path following, (b) steer angle, (c) path curvature, (d) yaw rate, and (e) rollover threshold.

Table 2 RMS and Max values of path following for conventional and extended MPC controllers

Controller	Speed/(m·s^{-1})	Steer angle/rad		Path curvature/(10^{-3} m^{-1})		Yaw rate/(rad·s^{-1})		LTR_d	
		RMS	Max	RMS	Max	RMS	Max	RMS	Max
Extended MPC	20	0.0173	0.0319	4.73	8.3	0.0949	0.1658	0.0822	0.1941
	30	0.0235	0.0464	4.74	8.5	0.1447	0.2795	0.2201	0.4778
Conventional MPC	20	0.0180	0.0557	4.86	16.8	0.0965	0.2112	0.0977	0.2739
	30	0.0247	0.0915	4.92	14.8	0.1510	0.3347	0.2565	0.5281

to simulate steering resistance. The dSPACE system compiles and embeds the vehicle–road dynamic model and control algorithm. Then, different strategies are generated to calculate steering angle command and send it to the actuator driver in real time.

A curve test driving at 30 m/s is performed on the HIL system, and the experiment results are shown in Fig. 11. A comparison is made in terms of path following, steering angle, path curvature, and lateral yaw dynamics with conventional and extended MPC controllers. The vehicle model and control parameters configured in the HIL system are not completely consistent with those set in the simulation environment. The steering angle is fed back by the sensor measurement, and other results are output by the embedded vehicle dynamics model, where the disturbance response mainly appearing in the steering angle is caused by communication delay and measurement noise. Figure 11(a) shows that the path trajectory with the conventional MPC control is strictly limited in the road centerline, which fails to use other drivable road areas comprehensively, whereas the extended MPC control strategy enables the autonomous vehicle to follow the optimal route within the road lane. Figures 11(b) and 11(c) show that the extended MPC control displays a smoother path following performance than the conventional one. Figure 11(d) shows that the lateral dynamics for the extended MPC control is maintained in a smaller envelope. By contrast, the oscillation of the conventional MPC controller at the corner conduces to the divergence of lateral dynamics. Apparently, the extended MPC control is more suitable for smooth path following of autonomous vehicles.

5 Conclusions

An extended MPC controller, which considers vehicle and road dynamics, is developed in this paper to find
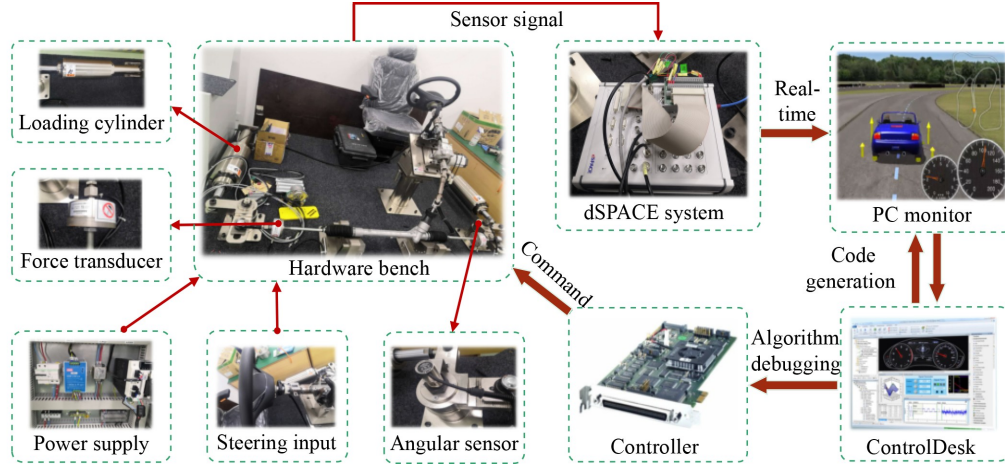
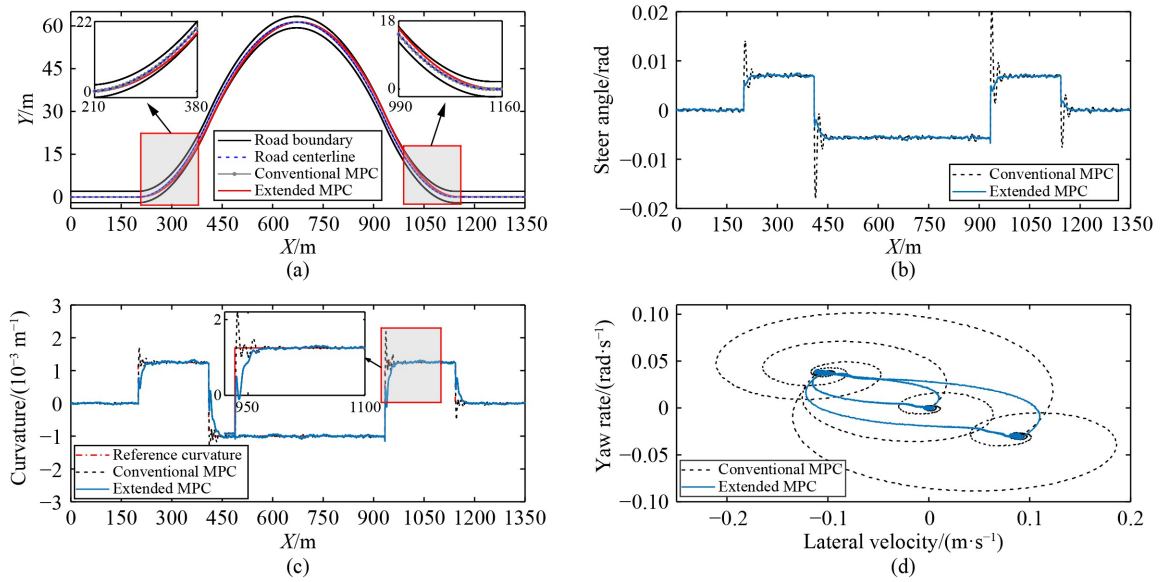**Fig. 10** HIL test system based on Simulink and dSPACE system.

Fig. 11 Experiment comparison results performed in HIL system: (a) path following, (b) steer angle, (c) path curvature, and (d) lateral velocity versus yaw rate.

autonomously the optimal driving path in the drivable road regions for smooth path following of autonomous vehicles. A vehicle dynamic model is created for accurately capturing the lateral motion and roll dynamics of the vehicle. Multiple constraints are concretely derived in the MPC controller formulation for stability and environmental envelopes. Then, the extended MPC method solved by DE optimization algorithm is proposed and takes the vehicle and road dynamics as a combined problem for smooth path following. Simulation and HIL experiments are conducted to verify the feasibility and the performance of the proposed extended MPC scheme. The results show that the proposed approach can obtain the optimal path following on the drivable road and satisfy the lateral dynamic stability constraints of the vehicle. It

can perform smooth transition steering on the road turns and maintain the path heading safely instead of crossing the road area in the road straight section. Smooth path following performance can be further enhanced for broader road drivable area and in coordination with human drivers. Moreover, the proposed method can effectively address the undesirable oscillations generated in constant speed turning. In the future work, to handle the complex turn conditions under variable speed operation, the longitudinal control with time-varying velocity and nonlinear tire model will be considered for the path following control with sharp turn behavior. Real vehicle experiments will also be conducted in a dynamic environment.

Nomenclature

C_{dj}, C_j, C_{0j}	Cornering stiffness coefficient
C_φ	Combined roll damping coefficient
CR	Crossover probability within [0, 1]
d_s	Desired minimum safe distance
D	Objective control input size
e_y	Lateral error
e_{yl}	Left road boundary
e_{yr}	Right road boundary
e_ψ	Heading error
Env_{max}	Maximum feasible road region
Env_{min}	Minimum feasible road region
f	Fitness function
F_{yf}	Lateral force of front tire
F_{yr}	Lateral force of rear tire
g	Gravitational acceleration
h	Distance from the spring mass to the roll center
I_x	Roll moment of inertia
I_z	Yaw moment of inertia
k	Discrete time
K_φ	Combined roll stiffness coefficient
l_f	Distance from center to front axle
l_r	Distance from center to rear axle
LTR	Lateral load transfer rate
LTR_d	Equivalent LTR
LTR_{max}	Maximum value of LTR_d
m	Total vehicle mass
m_s	Sprung vehicle mass
N_c	Control horizon
N_p	Prediction horizon
P	Population size
r	Vehicle yaw rate
$rand$	Random number with a uniform probability distribution in [0, 1]
rd	Randomly generated integral number in [1, 2, ..., D]
S	Driving path length
T_r	Vehicle track
T_s	Sample time
u_{ij}	New experimental input individual
v_{ij}	Mutation individual of $\Delta\delta_{fij}$
v_x	Longitudinal velocity
v_y	Lateral velocity
w	Vehicle width
x_0	Longitudinal position of vehicle origin
Δx	Distance between two adjacent points in x direction
y_0	Lateral position of vehicle origin
y_F	Lateral position of front axle

y_R	Lateral position of rear axle
Δy	Distance between two adjacent points in y direction
α_{hj}	Saturation slip angle
α_j	Tire slip angle
α_f	Front tire slip angle
α_r	Rear tire slip angle
α_t	Limit tire slip angle
β	Vehicle sideslip angle
δ_f	Front steer angle
δ_{fmax}	Maximum value of δ_f
δ_{fmin}	Minimum value of δ_f
ε	Slack variable
φ	Roll angle of vehicle
φ_r	Road bank angle
η_r	Robust mutation factor
κ	Reference road curvature
λ	Slack weight
σ	Penalty factor
ρ	Driving path curvature
ψ	Yaw angle
ψ_{ref}	Reference heading angle
$\Delta\delta_{fmax}$	Maximum of steer angle increment
$\Delta\delta_{fmin}$	Minimum of steer angle increment
$\Delta\delta_{fij}$	Initial individual
Γ_κ	Weight factor of ρ
Γ_s	Weight factor of S
Γ_u	Weight factor of Δu
Γ_ψ	Weight factor of e_ψ
A	Augmented state matrix
A_c	State matrix
A_d	Discrete state matrix
A_m	System state matrix
$\tilde{A}$	Predicted state matrix for output system
$\tilde{A}_h, \tilde{B}_{uh}, \tilde{B}_{vh}$	Coefficient matrices for hard constraints
$\tilde{A}_s, \tilde{B}_{us}, \tilde{B}_{vs}$	Coefficient matrices for soft constraints
$\tilde{A}_x$	Predicted state matrix
B_u	Augmented input matrix
B_{uc}	Input matrix
B_{ud}	Discrete input matrix
B_{um}	System input matrix
B_v	Augmented disturbance matrix
B_{vc}	Disturbance matrix
B_{vd}	Discrete disturbance matrix
B_{vm}	System disturbance matrix
$\tilde{B}_u$	Predicted input matrix for output system
$\tilde{B}_{ux}$	Predicted input matrix
$\tilde{B}_v$	Predicted disturbance matrix for output system
$\tilde{B}_{vx}$	Predicted disturbance matrix

C	Augmented output matrix
C_c	Output matrix
C_d	Discrete output matrix
E	Output deviation
E_1, E_2, E_{d2}	Constraint state matrix
F_1, F_2	Constraint input matrix
H_k, V_k, G_k, P_k	Quadratic transformation matrices
J_c	Conventional cost function
J_e	Optimized cost function
$J(Env)$	Penalty function of feasible road region
M	System matrix
M_1, M_2	Constraint output matrix
Q	Output weight matrix
R	Input weight matrix
u	Control input
u_{max}	Maximum value of u
u_{min}	Minimum value of u
U_i	Experimental control input sequence
Δu	Input increment
Δu_{max}	Maximum value of Δu
Δu_{min}	Minimum value of Δu
ΔU_c	Input variation
V_i	Mutation control input
W_i	Initial population
x	State vector
X_p	State prediction
y	Output vector
y_{hmax}	Hard constraint of upper output bound
y_{hmin}	Hard constraint of lower output bound
y_{max}	Maximum value of y
y_{min}	Minimum value of y
y_{ref}	Desired reference output
y_{smax}	Soft constraint of upper output bound
y_{smin}	Soft constraint of lower output bound
Y_p	Output prediction
Y_{ref}	Reference output matrix
γ	Disturbance input
ξ	Augmented state vector

References

1. Li K Q, Gao F, Li S E, Zheng Y, Gao H. Robust cooperation of connected vehicle systems with eigenvalue-bounded interaction topologies in the presence of uncertain dynamics. Frontiers of Mechanical Engineering, 2018, 13(3): 354–367

2. Spielberg N A, Brown M, Kapania N R, Kegelman J C, Gerdes J C. Neural network vehicle models for high-performance automated driving. Science Robotics, 2019, 4(28): aaw1975

3. Badue C, Guidolini R, Carneiro R V, Azevedo P, Cardoso V B, Forechi A, Jesus L, Berriel R, Paixão T M, Mutz F, de Paula Veronese L, Oliveira-Santos T, De Souza A F. Self-driving cars: a survey. Expert Systems with Applications, 2021, 165: 113816

4. González D, Pérez J, Milanés V, Nashashibi F. A review of motion planning techniques for automated vehicles. IEEE Transactions on Intelligent Transportation Systems, 2016, 17(4): 1135–1145

5. Guo J H, Luo Y G, Li K Q, Dai Y. Coordinated path-following and direct yaw-moment control of autonomous electric vehicles with sideslip angle estimation. Mechanical Systems and Signal Processing, 2018, 105: 183–199

6. Thrun S, Montemerlo M, Dahlkamp H, Stavens D, Aron A, Diebel J, Fong P, Gale J, Halpenny M, Hoffmann G, Lau K, Oakley C, Palatucci M, Pratt V, Stang P, Strohband S, Dupont C, Jendrossek L E, Koelen C, Markey C, Rummel C, van Niekerk J, Jensen E, Alessandrini P, Bradski G, Davies B, Ettinger S, Kaehler A, Nefian A, Mahoney P. Stanley: the robot that won the DARPA Grand Challenge. Journal of Field Robotics, 2006, 23(9): 661–692

7. Snider J M. Automatic steering methods for autonomous automobile path tracking. Dissertation for the Doctoral Degree. Pittsburgh: Carnegie Mellon University Pittsburgh, 2009

8. Morales J, Martínez J L, Martínez M A, Mandow A. Pure-pursuit reactive path tracking for nonholonomic mobile robots with a 2D laser scanner. EURASIP Journal on Advances in Signal Processing, 2009, (1): 935237

9. Chen Q Y, Sun Z P, Liu D X, Li X. Ribbon model based path tracking method for autonomous ground vehicles. Journal of Central South University, 2014, 21(5): 1816–1826

10. Zhang C Z, Hu J F, Qiu J B, Yang W, Sun H, Chen Q. A novel fuzzy observer-based steering control approach for path tracking in autonomous vehicles. IEEE Transactions on Fuzzy Systems, 2019, 27(2): 278–290

11. Marino R, Scalzi S, Netto M. Nested PID steering control for lane keeping in autonomous vehicles. Control Engineering Practice, 2011, 19(12): 1459–1467

12. Mohammadzadeh A, Taghavifar H. A robust fuzzy control approach for path-following control of autonomous vehicles. Soft Computing, 2020, 24(5): 3223–3235

13. Huang W, Wong P K, Wong K I, Vong C M, Zhao J. Adaptive neural control of vehicle yaw stability with active front steering using an improved random projection neural network. Vehicle System Dynamics, 2021, 59(3): 396–414

14. Zhao P, Chen J J, Song Y, Tao X, Xu T, Mei T. Design of a control system for an autonomous vehicle based on adaptive-PID. International Journal of Advanced Robotic Systems, 2012, 9(2): 44

15. Abdelhakim G, Abdelouahab H. A new approach for controlling a trajectory tracking using intelligent methods. Journal of Electrical Engineering & Technology, 2019, 14(3): 1347–1356

16. Guo J H, Hu P, Li L H, Wang R. Design of automatic steering controller for trajectory tracking of unmanned vehicles using genetic algorithms. IEEE Transactions on Vehicular Technology,

2012, 61(7): 2913–2924

17. Kritayakirana K, Gerdes J C. Using the centre of percussion to design a steering controller for an autonomous race car. Vehicle System Dynamics, 2012, 50(sup1 S1): 33–51

18. Kapania N R, Gerdes J C. Design of a feedback-feedforward steering controller for accurate path tracking and stability at the limits of handling. Vehicle System Dynamics, 2015, 53(12): 1687–1704

19. Chen W W, Zhao L F, Wang H R, Huang Y. Parallel distributed compensation/H$_\infty$ control of lane-keeping system based on the Takagi-Sugeno fuzzy model. Chinese Journal of Mechanical Engineering, 2020, 33(1): 61

20. Calzolari D, Schurmann B, Althoff M. Comparison of trajectory tracking controllers for autonomous vehicles. In: Proceedings of IEEE 20th International Conference on Intelligent Transportation Systems (ITSC). Yokohama: IEEE, 2017

21. Falcone P, Borrelli F, Asgari J, Tseng H E, Hrovat D. Predictive active steering control for autonomous vehicle systems. IEEE Transactions on Control Systems Technology, 2007, 15(3): 566–580

22. Falcone P, Borrelli F, Tseng H E, Asgari J, Hrovat D. Linear time-varying model predictive control and its application to active steering systems: stability analysis and experimental validation. International Journal of Robust and Nonlinear Control, 2008, 18(8): 862–875

23. Peng H N, Wang W D, An Q, Xiang C, Li L. Path tracking and direct yaw moment coordinated control based on robust MPC with the finite time horizon for autonomous independent-drive vehicles. IEEE Transactions on Vehicular Technology, 2020, 69(6): 6053–6066

24. Suh J, Chae H, Yi K. Stochastic model-predictive control for lane change decision of automated driving vehicles. IEEE Transactions on Vehicular Technology, 2018, 67(6): 4771–4782

25. Li Z J, Deng J, Lu R Q, Xu Y, Bai J, Su C Y. Trajectory-tracking control of mobile robot systems incorporating neural-dynamic optimized model predictive approach. IEEE Transactions on Systems, Man, and Cybernetics: Systems, 2016, 46(6): 740–749

26. Amer N H, Zamzuri H, Hudha K, Kadir Z A. Modelling and control strategies in path tracking control for autonomous ground vehicles: a review of state of the art and challenges. Journal of Intelligent & Robotic Systems, 2017, 86(2): 225–254

27. Song Y T, Shu H Y, Chen X B. Chassis integrated control for 4WIS distributed drive EVs with model predictive control based on the UKF observer. Science China. Technological Sciences, 2020, 63(3): 397–409

28. Tagne G, Talj R, Charara A. Design and comparison of robust nonlinear controllers for the lateral dynamics of intelligent vehicles. IEEE Transactions on Intelligent Transportation Systems, 2016, 17(3): 796–809

29. Chowdhri N, Ferranti L, Iribarren F S, Shyrokau B. Integrated nonlinear model predictive control for automated driving. Control

Engineering Practice, 2021, 106: 104654

30. Guo H Y, Liu J, Cao D P, Chen H, Yu R, Lv C. Dual-envelop-oriented moving horizon path tracking control for fully automated vehicles. Mechatronics, 2018, 50: 422–433

31. Beal C E, Gerdes J C. Model predictive control for vehicle stabilization at the limits of handling. IEEE Transactions on Control Systems Technology, 2013, 21(4): 1258–1269

32. Ji J, Khajepour A, Melek W W, Huang Y. Path planning and tracking for vehicle collision avoidance based on model predictive control with multiconstraints. IEEE Transactions on Vehicular Technology, 2017, 66(2): 952–964

33. Li X H, Sun Z P, Cao D P, Liu D, He H. Development of a new integrated local trajectory planning and tracking control framework for autonomous ground vehicles. Mechanical Systems and Signal Processing, 2017, 87: 118–137

34. Merabti H, Belarbi K, Bouchemal B. Nonlinear predictive control of a mobile robot: a solution using metaheuristcs. Journal of the Chinese Institute of Engineers, 2016, 39(3): 282–290

35. Brown M, Funke J, Erlien S, Gerdes J C. Safe driving envelopes for path tracking in autonomous vehicles. Control Engineering Practice, 2017, 61: 307–316

36. Guo H Y, Liu F, Xu F, Chen H, Cao D, Ji Y. Nonlinear model predictive lateral stability control of active chassis for intelligent vehicles and its FPGA implementation. IEEE Transactions on Systems, Man, and Cybernetics: Systems, 2019, 49(1): 2–13

37. Du X X, Htet K K K, Tan K K. Development of a genetic-algorithm-based nonlinear model predictive control scheme on velocity and steering of autonomous vehicles. IEEE Transactions on Industrial Electronics, 2016, 63(11): 6970–6977

38. Guo H Y, Shen C, Zhang H, Chen H, Jia R. Simultaneous trajectory planning and tracking using an MPC method for cyber-physical systems: a case study of obstacle avoidance for an intelligent vehicle. IEEE Transactions on Industrial Informatics, 2018, 14(9): 4273–4283

39. Cao H T, Song X L, Zhao S, Bao S, Huang Z. An optimal model-based trajectory following architecture synthesising the lateral adaptive preview strategy and longitudinal velocity planning for highly automated vehicle. Vehicle System Dynamics, 2017, 55(8): 1143–1188

40. Di Cairano S, Tseng H E, Bernardini D, Bemporad A. Vehicle yaw stability control by coordinated active front steering and differential braking in the tire sideslip angles domain. IEEE Transactions on Control Systems Technology, 2013, 21(4): 1236–1248

41. Xiao L J, Wang M, Zhang B J, Zhong Z. Vehicle roll stability control with active roll-resistant electro-hydraulic suspension. Frontiers of Mechanical Engineering, 2020, 15(1): 43–54

42. Liu Q J, Chen W, Hu H S, Zhu Q, Xie Z. An optimal NARX neural network identification model for a magnetorheological damper with force-distortion behavior. Frontiers in Materials, 2020, 7: 10